



Fermi National Accelerator Laboratory

FERMILABPub-94/110

8.9 GeV \bar{p} Yield Measurements at the Fermilab Antiproton Source

S.C. O'Day and F.M. Bieniosek

***Fermi National Accelerator Laboratory
P.O. Box 500, Batavia, Illinois 60510***

May 1994

Accepted by ***Nuclear Instruments and Methods***



Disclaimer

This report was prepared as an account of work sponsored by an agency of the United States Government. Neither the United States Government nor any agency thereof, nor any of their employees, makes any warranty, express or implied, or assumes any legal liability or responsibility for the accuracy, completeness, or usefulness of any information, apparatus, product, or process disclosed, or represents that its use would not infringe privately owned rights. Reference herein to any specific commercial product, process, or service by trade name, trademark, manufacturer, or otherwise, does not necessarily constitute or imply its endorsement, recommendation, or favoring by the United States Government or any agency thereof: The views and opinions of authors expressed herein do not necessarily state or reflect those of the United States Government or any agency thereof.

8.9 GeV \bar{p} yield measurements at the Fermilab antiproton source **

S.C. O'Day *, F.M. Bieniosek

Fermi National Accelerator Laboratory, P.O. Box 500, Batavia, IL 60510, USA

(Received 3 November 1993)

The \bar{p} yield at 8.89 ± 0.18 GeV has been measured for different lithium collection lens gradients and lens to target distances. Using an empirical \bar{p} production and collection model, the yield as a function of production angle and vertex position in the target has been extracted. Data taken for different targets indicates that the \bar{p} yield varies little as a function of atomic weight. A reduction in the Re target yield due to target melting was measured for the nominal proton intensity on target. An enhancement in Cu \bar{p} production was observed for proton beam targeted very near the interface with a lighter material (Al) disk.

1. Introduction

The Fermilab Antiproton Source [1] and Target Station [2] are shown in Figs. 1a and 1b, respectively. In typical \bar{p} production running, a 120 GeV beam of 1.6×10^{12} protons per pulse (80 full bunches per pulse) impinges on a target. The target assembly consists of a stack of Ni, Cu, Al and powdered Re (rhenium) cylindrical disks mounted on a moveable shaft. A target is selected by moving the shaft vertically; the target length and distance to the lens is adjusted by moving the shaft in the horizontal plane. A lithium lens [3] downstream of the target collects and focuses the 8.9 GeV/c secondaries. The distance from the center of the target to the upstream edge of the collection lens which maximizes the \bar{p} yield is typically 17-21 cm. This distance diminishes as the current through the lens, and thus the magnetic field gradient, rises. The secondaries travel another 60 cm after leaving the lens before being kicked 3" horizontally by a pulsed dipole into the aperture of the AP2 beamline. The AP2 beamline transports the beam to the Debuncher storage ring.

The optimization of \bar{p} production and collection requires a detailed understanding of the way various factors affect the \bar{p} yield. The data presented in this paper will impact the design changes which must take place in order for the target station to operate after the Fermilab Main Injector project is completed. As well, in upgrading and adding to the existing target station instrumentation and devices, it is important to

know how to weigh predicted gains in instantaneous yield versus potential system reliability problems.

To maximize the number of \bar{p} 's produced, one would like the proton intensity to be as large as possible. The proton intensity is limited not only by the performance of the Main Ring but also by considerations of target survival. There is a material dependent limit on energy deposition. Exceeding this limit for a particular target type will result in instantaneous melting and perhaps stress wave fractures.

To maximize the lithium collection lens acceptance, the lens to target distance at focus must be minimized. This is accomplished by operating the lens at the highest feasible current. Higher lens currents result in greater thermal stresses on various collection lens components due to Joule heating. As well, a shorter lens to target distance increases the radiation exposure of the lens transformer resulting in greater heating of the transformer core. These effects limit the lifetime of lenses operating at extremely high field.

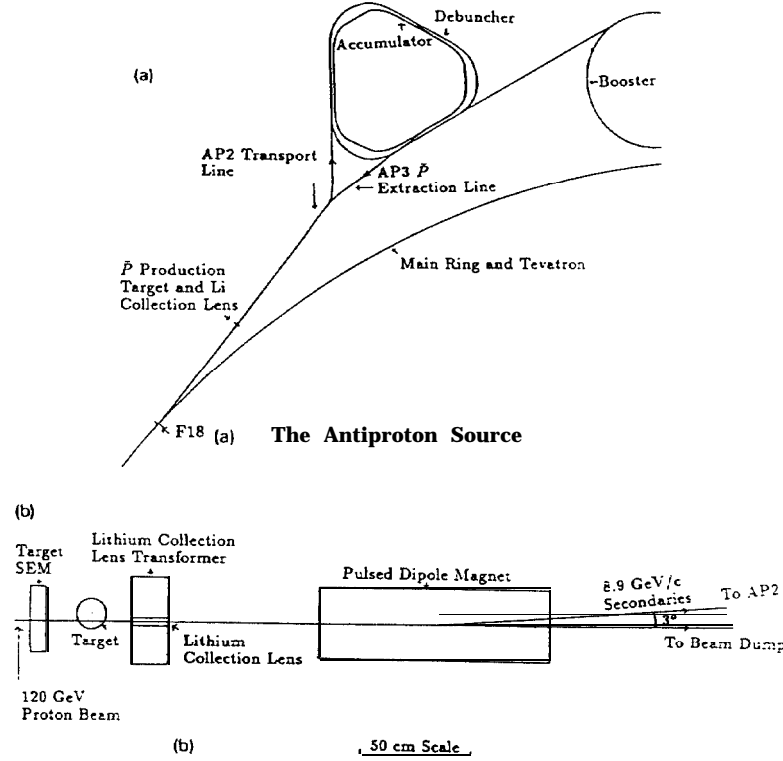
Under the best of running conditions, the absolute yield into the Debuncher was measured to be $1.95 \times 10^{-5} \bar{p}/p$ or 4.1 μA of circulating current per pulse. At that time, the collection lens to target distance was 17 cm and the Main Ring delivered 2.1×10^{12} protons per pulse on target.

2. Monte Carlo production and collection model

In order to extract the collection lens acceptance and make predictions from fits to the data, an empirical Monte Carlo model was written based on the work of Hojvat and Van Ginneken [4]. This model includes

* Corresponding author.

** Work supported by the US Department of Energy under contract No. DE-AC02-76CH03000.



Antiproton Source Target Station

Fig. 1. (a) Fermilab Antiproton Source. (b) Antiproton Source Target Station.

primarily and secondarily produced \bar{p} s in an admixture defined by the user. In standard running, the secondary contribution is set to 15% for Cu and to 25% for W with interpolation for intermediate values of A (atomic weight).

The primary \bar{p} vertex distribution along the beam direction (z) follows the exponential decline of the proton intensity

$$P(z) = e^{-(z+z_l/2)/L_{abs}} \quad (1)$$

where z_l is the target length and $z = 0$ is the target center. The secondary \bar{p} vertex distribution implemented follows the relationship:

$$S(z) = S_0(1 - e^{-(z+z_l/2)/L_{abs}})(1 - S_1 e^{-(z_l/2-z)/L_{pi}}). \quad (2)$$

L_{abs} is the proton absorption length and L_{pi} is the pion absorption length. The expression consists of two factors. The first is proportional to the number of protons which have interacted in the target. The second factor is proportional to the number of produced pions which interact in the target. By varying the

parameters S_0 and S_1 one may move the secondary \bar{p} vertex distribution upstream or downstream.

Once a vertex position along the beam direction is established, random Gaussian production angle and transverse vertex coordinates are assigned. Each \bar{p} is tracked to the target edge with Coulomb multiple scattering and \bar{p} reabsorption taken into account. The tracking then continues to the upstream face of the lithium collection lens where a radial acceptance cut is applied. The tracking through the lens is described below. Admittance cuts are applied after lens tracking is complete. The standard Monte Carlo model parameters are shown in Table 1.

The lithium lens used to collect the antiprotons is a cylindrical conductor of radius r_0 carrying a total current I . The magnetic induction B is ideally a linear function of radius r , $B(r) = \mu_0 I r / 2 \pi r_0^2$. Such an ideal lens is in focus when the distance from the target center to the upstream face of the lens is

$$Z_{lens-target} = 1/(k \tan(kl)), \quad (3)$$

where $k = \sqrt{0.3G/p}$, l = lens length, and G is the

field gradient $B(r)/r$. But in practice the current is pulsed to minimize Joule heating in the lithium core. A pulsed power supply delivers a damped half-sine wave current to the lens described by $I(t) = I_0 \exp(-\alpha t) \sin(\omega t)$ ($0 < \omega t < \pi$) where I_0 is the peak current without damping, α is the damping constant, and ω is the angular frequency determined by the capacitance and inductance of the pulser circuit. The current and magnetic field diffuse into the lithium core on a time scale that depends on the ratio of the skin depth to the lens radius δ/r_0 . The field strength varies as a function of time according to [5]

$$B(r, t) = B_0 \operatorname{Re} \left\{ \frac{i J_1(\beta r)}{J_1(\beta r_0)} e^{-\gamma t} \right\} + \sum_j a_j J_1(\lambda_j r) e^{-\lambda_j^2 t / \sigma \mu}, \quad (4)$$

where $\gamma = \alpha + i\omega$ and B_0 is the maximum value of B for an undamped pulse. $J(\beta r)$ is a first order Bessel function with complex argument βr and with β defined by $\beta^2 = \sigma \mu \alpha + 2i/\delta^2$. $\lambda_j r_0$ is a root of the first order Bessel function $J_1(x) = 0$. The a_j coefficients are given by

$$a_j = -4B_0 \frac{r_0^2}{\delta^2} \frac{\lambda_j r_0}{(\lambda_j^2 - \sigma \mu \alpha)^2 r_0^4 + 4(r_0/\delta)^4} \frac{1}{J_0(\lambda_j r_0)}. \quad (5)$$

The resulting deviation from linearity may be seen in Fig. 2. The ratio $B(r)/r$ as a function of radius r is plotted for three values of phase $\phi = \omega t$. The power supply voltage is 2625 V, and the gradient of the linear

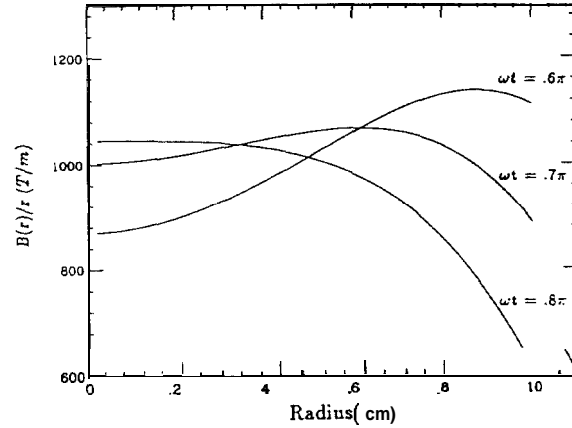


Fig. 2. $B(r)/r$ vs radius for three different collection lens current pulse phases $\phi = \omega t$.

component of the field [5] is $\langle G \rangle = 1000$ T/m at $\phi = 0.7\pi$.

Aberrations in the lens optics caused by nonuniform penetration of the magnetic field have a strong effect on yield [6]. The realistic variations in magnetic field strength are included in the model. The path of particles is traced through the lens in four steps, and the deflection in each step is calculated using the field in the respective region.

3. Measurements

3.1. Measurement tools

The secondaries transported down the AP2 beamline into the Debuncher (predominantly electrons and pions (7)) were measured just before injection into the Debuncher using an ionization chamber (IC728). The first opportunity to measure the \bar{p} flux directly arises only after the electrons have stopped circulating due to synchrotron radiation and the other particles have decayed. Thus, \bar{p} yield measurements were made in the Debuncher by using both a dynamic signal analyzer (dsa) and a dc beam current transformer (dcct). The signal analyzer does a fast Fourier transform of the longitudinal Schottky power spectrum and integrates it over a specified bandwidth. The signal analyzer is calibrated to the dcct and is accurate to a few percent.

3.2. Dependence of yield on lens timing

Measurements were made to investigate the dependence of yield on the beam passage time relative to the phase of the lens current pulse. The instrumentation used consisted of an ionization chamber located near the end of the AP2 beamline and a dcct in the De-

Table 1
Standard Monte Carlo parameters

Parameter	Value
Lens radius [m]	0.01
Lens length [m]	0.15
Lens to target distance [m]	0.17
Lens power supply voltage [V]	2342
Phase of current pulse	0.7π
a [s^{-1}]	1800
δ [m]	0.00455
Circuit capacitance [μF]	4.5×10^3
Target disk radius [m]	0.05
Target material	Ni
Target size [m]	0.02
AP2/Debuncher admittance [π mm mRad]	26
\bar{p} central p [GeV/c]	5.89
$\bar{P} a_{\perp}$ [GeV/c]	0.17s
Half-angle of primary production [rad]	0.07
Half-angle of secondary production [rad]	0.1
Proton beam $\sigma_x = \sigma_y$ [m]	0.00015
S_0	9
S_1	0.7

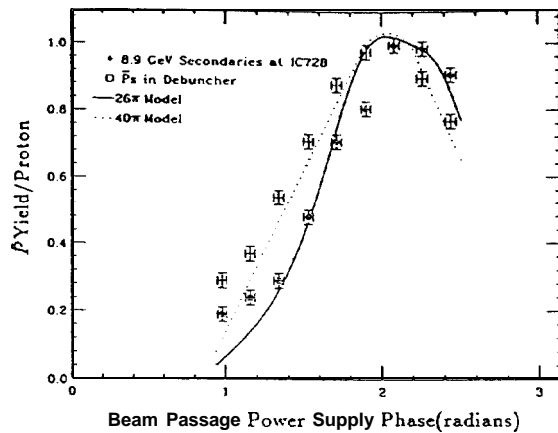


Fig. 3. Yield to IC728 and into the Debuncher vs lens current pulse phase ϕ at which the beam passes. The yields are normalized to unity.

buncher. As noted above, the ionization chamber measurement is dominated by pions and electrons while the **dcct** measurement is made primarily on \bar{p} s.

Results are shown in Fig. 3, together with model predictions for two admittances, normalized to the data. The peak of the yield curve depends on the aperture of the acceptance optics downstream of the lens because of the inward penetration of the focusing field in the lens. The peak field gradient moves inward with time during the pulse; different apertures sample different portions of the field. The model predictions shown in the figure are for a lens which is in focus. As the lens-target distance is increased, the predicted yield **curve** becomes smaller and narrower in time; as the lens-target distance is decreased, the curve broadens and splits into a double-peaked distribution. The ionization chamber yield curve shows agreement with a model prediction in the **range** of 40π mm mrad, while

the Debuncher yield **curve** has a fit in the **range** $20\text{--}26\pi$ mm mrad. Shown is the 26π prediction. The difference **between** the curves indicates that the \bar{p} s pass through a **more restrictive aperture** downstream of the first point of measurement. The measured aperture into the Debuncher agrees with an independent direct measurement of Debuncher **aperture** (26π), but leaves open the possibility that the AP2 beamline may have an **aperture** restriction between the ionization chamber and the Debuncher. Discrepancies **between** the data and the model at early times may be due to the enhanced tail on the multiple Coulomb scattering distribution, which is not well modelled by a Gaussian distribution. Due to limitations in the timing circuit, phases **larger** than 0.8π were not achievable.

3.3. Geometrical yield darn

The measured \bar{p} yield versus target to lens distance for different lens power supply voltages is plotted in Figs. 4a and 4b. The predicted yield **curves** were normalized to the highest voltage data. The production half-angle parameters given in Table 1 were found by matching the model to the data. Yield predictions for the ideal and realistic lens fields are compared in Fig. 5 for the 2342 V data. The agreement with the data is better for the realistic lens. The impact of the realistic lens field on the predicted vertex distribution is shown in Fig. 6. For the design lens gradient (G) = 1000 T/m, the realistic lens accepted vertex distribution is shifted downstream with respect to the ideal lens. The production angle distribution which comes from the model is shown in Fig. 7.

The yield as a function of power supply voltage is given in Fig. 8 along with model predictions for different AP2/Debuncher admittances. The data shown correspond to $\langle G \rangle$ in the range of 620–890 T/m. For the purposes of this plot, the yield data and model curves

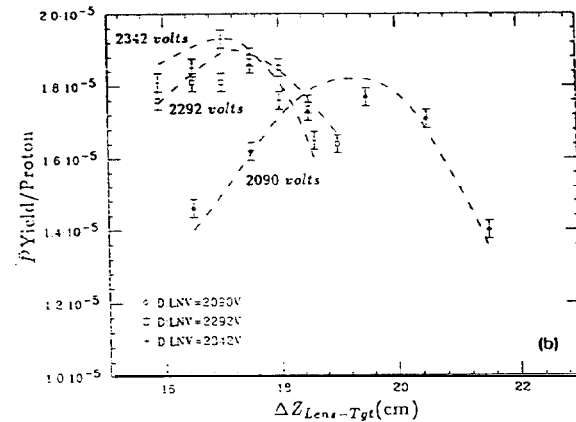
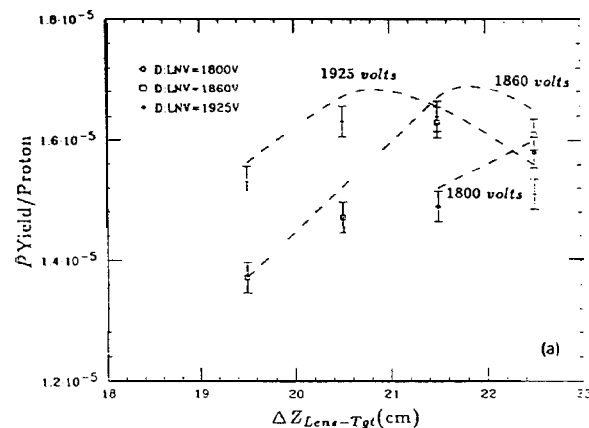


Fig. 4. \bar{p} yield vs lens to target distance for lens power supply voltages (a) 1800, 1860, 1925 V and (b) 2090, 2292, 2342 V.

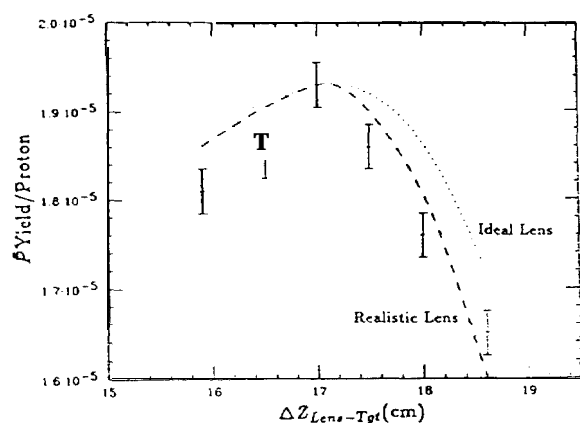


Fig. 5. \bar{p} yield vs lens to target distance for a lens power supply voltage of 2342 V. Ideal and realistic lens model fits are shown.

were normalized using a 26π mm mrad admittance. The true admittance is known to only a few π mm mrad so that this curve is useful only to predict relative dependence of yield on admittance. However, since the voltage is known to 1%, accurate scaling predictions are possible.

Extrapolating the measured yield at 2342 V (Fig. 4) to $\langle G \rangle = 1000$ T/m (Fig. 2) gives a predicted yield of 2.06×10^{-5} \bar{p}/p . This is lower than the Hojvat and Van Ginneken [4] prediction for a 5 cm W target of 6.8×10^{-5} under similar conditions. The 0 $^\circ$ production

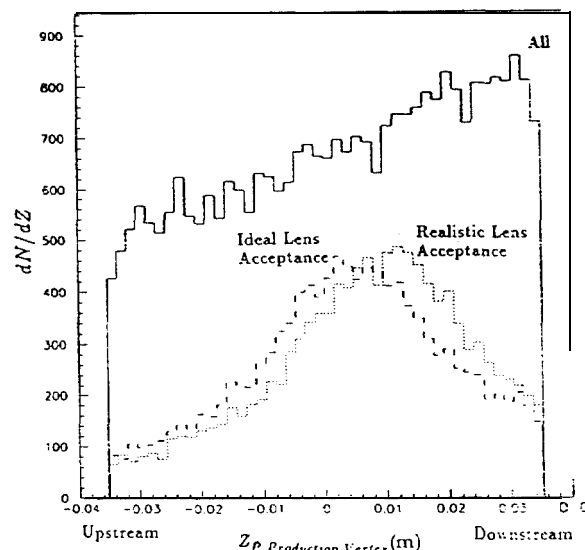


Fig. 6. dN/dZ (unnormalized) vs Z (\bar{p} production vertex) for $\langle G \rangle = 1000$ T/m. The curve marked "ALL" includes particles which would otherwise be removed by the 26π mm mrad admittance cut. The two lower curves show the ideal and realistic lens model acceptance

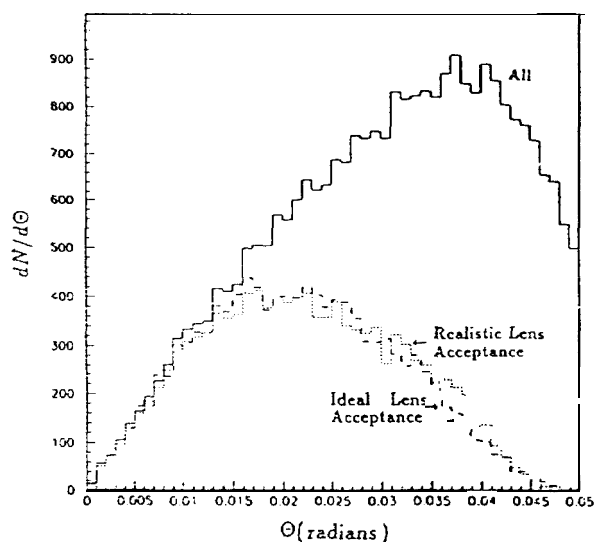


Fig. 7. $dN/d\theta$ (unnormalized) vs θ (\bar{p} production) for $\langle G \rangle = 1000$ T/m. The curve marked "ALL" includes particles which would otherwise be removed by the 26π mm mrad admittance cut. The two lower curves show the ideal and realistic lens model acceptance.

angle value of $(1/\sigma)(d\sigma/d\Omega dp) = 0.252\bar{p}/(\text{sr GeV}/c)$ used by Hojvat and Van Ginneken was found by extrapolating then existing data into the forward \bar{p} production region. The original model was later updated along with the MARS10 program to better match Fermilab \bar{p} yield data from 1986 as well as the FLUKA86 program [8].

3.4 Target material yield data

No statistically significant differences in the \bar{p} yield from Cu, Ni and Re have been observed. This result

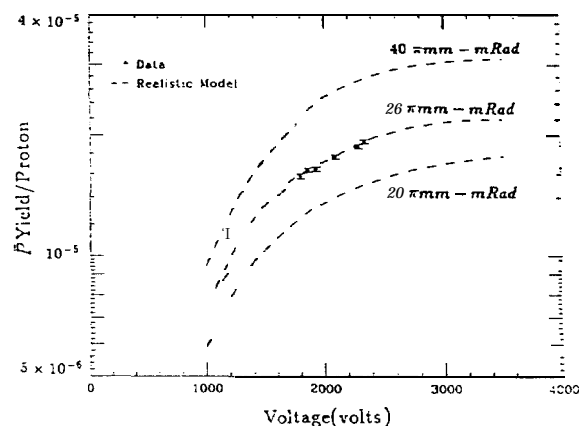


Fig. 8. \bar{p} yield vs collection lens power supply voltage

differs slightly from previous measurements which showed that W provided 5% more yield than Cu [8]. The fact that the Re target was powdered and thus had 73% of the density of solid Re may explain the difference since Re and W are very similar in atomic weight. The fact that all three targets had similar optimum target lengths implies that \bar{p} production and \bar{p} absorption rates were also similar. The measured optimum effective target length was found to be 7.0 ± 0.1 cm for Cu and Ni. The optimum Re length was 6.85 ± 0.1 cm.

The model was used with secondary \bar{p} production turned off in order to estimate the difference in secondary contributions to the yield of the two targets. The model predicts that the Re primary contribution is 15% less than that of Cu. Since the data indicate that the overall yields are identical, one may conclude that the difference comes from secondaries. The absorption cross sections used in the model [9] are believed to be quite reliable and give us confidence in this result.

3.5 Target density depletion data

A large energy deposition on target is expected to locally melt target materials. As the target material melts, its density drops, which results in a diminished hadron yield from those bunches of protons which arrive after this melting has occurred. Data were taken using rhenium and nickel targets which have melting point energies of 600 and 1100 J/g respectively.

The Fermilab Main Ring provided a beam with an intensity of 1.6×10^{12} protons per pulse and a transverse width (σ) of 0.14 mm on target. Using a resistive wall monitor in the Debuncher, the bunch structure of the beam during the first turn was measured. A similar wall monitor was used to measure the incoming proton bunch structure. By integrating the individual bunches, the charge associated with each bunch was determined. Comparing the bunch charge with the corresponding proton bunch charge provided a measure of the yield on a bunch-by-bunch basis. The charge in arbitrary units for protons on target and first turn particles in the Debuncher as a function of bunch number is given in Fig. 9 for a Re target. The yield from the last 25% of the bunches shows an obvious deficit which increases with bunch number. By the eightieth bunch, the yield is down $8\% \pm 4\%$ as compared with the first.

Two models were employed to help understand the relationship between the bunch number at which the yield began to drop, the beam region temperature and the melting point energy. First, the bunch number at which the yield from Re began to drop was 45 ± 5 . This corresponds to a CASIM calculated melting point energy of 600 ± 65 J/g and is consistent with the thermodynamic prediction of 600 J/g. Second, a model which assumes a 25% beam absorption rate and the relationship $d\rho/dT = -0.0001\rho$ for liquid rhenium

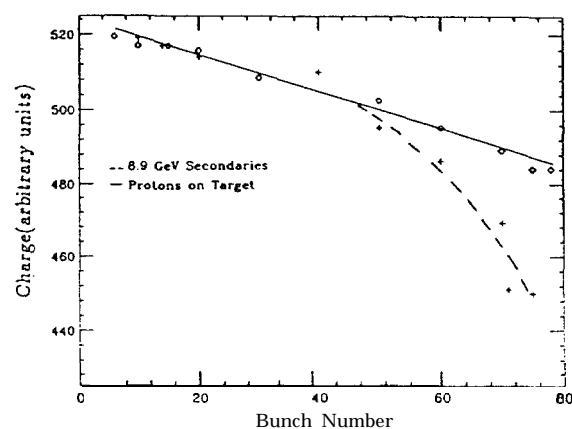


Fig. 9. Charge per bunch vs bunch number (Re target).

predicts that $\Delta\rho/\rho = -21\%$. Since rhenium melts at 3180°C the density drop given corresponds to a temperature of 5280°C . This implies that the melting began after 60% of the pulse hit the target and is consistent with the data.

Target density depletion was not observed in Ni. This is what one would expect since the energy deposition in Ni for an intensity of 1.6×10^{12} protons per pulse is 615 J/g while the melting point energy is 1100 J/g.

3.4 Edge enhancement of yield

The relative importance of material and geometry dependent factors such as \bar{p} production and reabsorption, Coulomb multiple scattering and the secondary production of \bar{p} s was investigated further by studying yield near the interface of two dissimilar materials. Since the vertical motion of the target assembly permits the beam to impinge upon different portions of the target stack, it was possible to do a \bar{p} yield measurement at both interfaces of an Al disk sandwiched between two Cu disks. The results are shown in Fig. 10. The edge enhancement of yield is observed when the lens is focused on the upstream portion of the target where the \bar{p} path lengths in the dissimilar materials are longer. A 5% yield enhancement in Cu and a 5% yield reduction in Al was observed under these conditions in agreement with model predictions. The enhancement in Cu is due to the reduced scattering and reabsorption of \bar{p} s created in the dense Cu material but which escape through the lighter Al material. The converse is true for \bar{p} s produced in the Al. The significance of this result is twofold. First, the results show that secondary production must be a relatively small contribution to total yield, since it would be expected to mask the edge enhancement effect. Second, the demonstration of the edge enhancement ef-

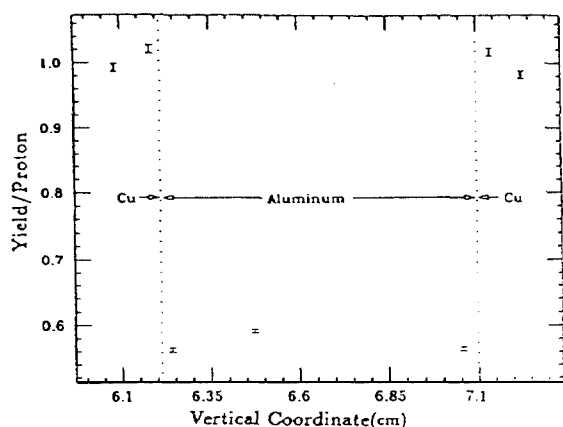


Fig. 10. Yield enhancement at the target vertical edge. The yield is normalized to unity.

fect indicates that it may be possible to increase the yield by designing a target that utilizes this result (see below).

4. Discussion

As a result of these measurements and the Monte Carlo simulation work done, gains in \bar{p} yield made by increasing the lens gradient are predictable. The work builds on previous Monte Carlo \bar{p} production calculations by adding a realistic simulation of the collection lens magnetic field. This model is used to fit data taken at a higher proton beam intensity and a higher lens field gradient than had been achieved previously. By varying the timing of the lens current pulse, it has been possible to independently measure the Debuncher and AP2 beamline apertures. By tuning the production angle parameters in the program to fit the data, it has been possible to extract \bar{p} production angle and target vertex distributions. Finally, it was possible to use all of this information together to predict the scaling of yield to collection lens field gradients higher than those achieved to date.

The Hojvat and Van Ginneken predictions for a 5 cm W target are higher than a fit to the Ni and Cu \bar{p} yield data extrapolated to the lens design gradient by a factor of 3.3 to 3.8. As well, the W yield data is expected to be 1.4 times higher than Cu or Ni based on Hojvat and Van Ginneken, but only 1.05 times higher according to Azhgirey and Mokhov. Thus, the zero production angle value of $(1/\sigma)(d\sigma/d\Omega dp) = 0.252\bar{p}/(\text{sr GeV}/c)$ used in the Hojvat and Van Ginneken model should be scaled down to a value of between 0.07 and 0.1 $1\bar{p}/(\text{sr GeV}/c)$ depending on the assumptions used. It should be noted that the optimum yield for the realistic lens is within a few percent of the yield for an ideal lens. It is on this basis that direct

comparisons between the data and the previous models have been made.

Measured yield is independent of A for the target materials studied here using the described target geometry. Although the yield from proton-nucleon inelastic scattering for higher A materials rises with the proton absorption cross section ($\sigma_{\text{absorption}} = 38.2 \text{ mbA}^{-1/3}$) [9,10] and the secondary yield from produced pions and neutrons is higher as well, a greater fraction of produced \bar{p} s is absorbed to compensate. In order to reduce this absorption, one might use a wire target. The model presented here indicates that a cylindrical Ni target with a diameter of 0.5 mm will increase yield by 20% compared with the presently used thick target disk. The results of the study showing yield enhancement at the Al/Cu interface lend confidence to this prediction.

In high-intensity \bar{p} production target operation Ni is the target material of choice because of a combination of its high melting point energy, superior yield strength and resistance to damage by shocks. Ni has a relatively high melting point energy (1100 J/g). The yield strength of Ni (230000 Pa) is competitive with other target materials such as Re (270000 Pa) and Cu (72000 Pa). Further, a Ni target can be expected to undergo relatively modest beam-induced mechanical stresses. This is due to the fact that, in Ni, the ratio of instantaneous overpressure to beam energy input $dP/dE = \rho\Gamma = 15800 \text{ Pa kg/J}$, where ρ is the density, and Γ is the Gruneisen parameter, is low, particularly with respect to W and Re. An analysis of stress wave behavior in targets is given elsewhere [11].

According to Hojvat and Van Ginneken, the \bar{p} yield rises as the proton spot size on target decreases. The energy deposition per gram of material in the beam as a function of spot size has been calculated [12]. The slope of the yield versus spot size curve has not been measured carefully. This measurement will be made in the 1993-1994 collider run using a high resolution secondary emission monitor which will be located just upstream of the target. The introduction of a beam sweeping system to handle Main Injector intensities will insure that the spot size can be minimized without melting the target [13].

Acknowledgement

The authors are grateful for the contribution of Michael Gormley to the work described in this paper.

References

- [1] IEEE Trans. Nucl. Sci. 30 (1983) 1970.
- [2] C. Hojvat et al., IEEE Trans. Nucl. Sci. 30 (1983) 2815.

- [3] J.A. MacLachlan et al., IEEE Trans. Nucl. Sci. 28 (1981) 278.5.
- [4] C. Hojvat and A. Van Ginneken, Nucl. Instr. and Meth. 206 (1983) 67.
- [5] A.J. Lennox, IEEE Trans. Nucl. Sci. 30 (1983) 3663.
- [6] G. Dugan et al., ibid., p. 3660.
- [7] Bross et al., Nucl. Instr. Meth. A 332 (1993) 27.
- [8] I.L. Azhgirey and N.V. Mokhov, Fermilab TM-1529 (1988).
- [9] Carroll et al., Phys. Lett. B 80 (1979).
- [10] T. Roberts, H. Gustafson, L. Jones. M. Longo and M. Whalley, Nuc. Phys. B 159 (1979) 56.
- [11] Z. Tang and K. Anderson, Fermilab TM-1763 (1991).
- [12] C. Bhat and N. Mokhov. Fermilab-TM-1585 (1989).
- [13] F.M. Bicniosek. Fermilab-TM-1857 (1993).